PAPER

Check for updates

Ambient-processed semitransparent perovskite solar cells from eco-friendly solvents

Cyril C. F. Kumachang, [a] Brittlee G. Reese,[a] Tawanda J. Zimudzi, [b] Ivy M. Asuo *[a] and Nutifafa Y. Doumon *[abc]

The development of semitransparent perovskite solar cells is crucial for applications in building-integrated photovoltaics, agrivoltaics, and tandem solar cells. However, optimizing their efficiency while maintaining high transparency and employing eco-friendly solvents remains challenging. In this work, we investigate the impact of solvent engineering and processing conditions on the structural, optical, and photovoltaic properties of perovskite thin films. First, we demonstrate that dimethyl sulfoxide (DMSO), an eco-friendly solvent, can be used as a standalone alternative to the widely used and hazardous N,N-dimethylformamide:DMSO co-solvent system for ambient-processed $FA_{0.77}MA_{0.23}PbI_{2.74}Cl_{0.26}$ perovskite. We also assess the effects of antisolvent treatments (IPA and EtOH) on crystallinity, charge carrier dynamics, and device performance. Additionally, we show that reducing the gold electrode thickness from 80 nm to 30 nm significantly enhances device-level transparency, as confirmed through full-stack optical measurements. We achieve a power conversion efficiency of up to 10.9% and demonstrate semitransparency, with a light utilization efficiency (LUE) exceeding 4.26% in 30 nm gold top electrode DMSO-only devices, using solely thin-film transmittance. Using the full device stack, the semitransparent devices yield a LUE of 0.59%, highlighting the inadequacy of relying solely on thin-film transmittance. Notably, DMSO-based devices exhibit superior semitransparency and sustainability despite lower efficiencies. Our findings highlight a viable pathway to scalable, eco-friendly, ambient-processed semitransparent perovskite solar cells that balance efficiency, transparency, and environmental considerations for future energy applications.

[a] *Department of Materials Science and Engineering, The Pennsylvania State University, University Park, PA, 16802, USA. E-mail: ipa5154@psu.edu, nzd5349@psu.edu*

[b] *Materials Research Institute, The Pennsylvania State University, University Park, PA, 16802, USA*

[c] *Department of Engineering Science and Mechanics, The Pennsylvania State University, University Park, PA, 16802, USA*

1. Introduction

Since the emergence of metal halide perovskite (MHP) photovoltaics (PVs) in 2009, with a modest power conversion efficiency (PCE) of 3.8%, they have garnered considerable attention and experienced rapid growth in the field of emerging PV research.[1–3] This is due to their unique properties, including an extended exciton diffusion length, tunable bandgap, broad light absorption across the visible spectrum, solution processability, and low-cost precursor materials.[3] These attractive properties of MHPs have facilitated their application in photovoltaics and optoelectronic devices, such as light-emitting diodes (LEDs),[4] photodetectors[5,6] photovoltaics (including indoor photovoltaics (IPVs),[7] semitransparent photovoltaics (ST-PVs),[8] *etc.*), and related technologies.[9] As reported in the

best research-cell chart by the National Renewable Energy Laboratory, the certified PCE of single-junction metal halide perovskite photovoltaics (MHP-PVs) has progressed from 14.1% in 2013 to 27.0% in 2025, while the literature recorded 27.3% lab-level efficiency, underscoring the solar energy harvesting potential of this emerging PV technology.[10–13] However, challenges, including their susceptibility to degradation under heat, moisture, light, electrical bias,[14,15] reliance on the toxic element lead (Pb),[16,17] and the use of environmentally harmful solvents during processing, limit the commercialization of MHP-PVs.[18,19]

Over the years, N,N-dimethylformamide (DMF) and dimethyl sulfoxide (DMSO) have become widely used as co-solvents for dissolving MHP precursors. While these solvents contribute to the formation of high-quality perovskite films – owing to their high solubility, favorable vapor pressure, moderate surface tension, and annealing temperatures, which in turn enhance photovoltaic performance – their toxic environmental impact raises significant concerns regarding health and sustainability.[20,21] DMF, widely employed for perovskite layer deposition, is listed as a substance of very high concern under the European Chemicals Agency's REACH regulation due to its acute toxicity,

reproductive health risks, and potential for liver damage.[18,22] As part of Regulation (EU) 2021/2030, the European Union imposed restrictions on the industrial and professional use of DMF, effective December 2023.[23,24] This decision was based on comprehensive risk assessments that highlighted the need for safer alternatives, aligning with the EU's broader goal of reducing reliance on hazardous chemicals through sustainable chemical management.[23] Additionally, solvents such as N,N-dimethyl-acetamide (DMAC), N-methyl-2-pyrrolidone (NMP), gamma-butyrolactone (GBL), 1,3-dimethyl-3,4,5,6-tetrahydropyrimidin-2($1H$)-one (DMPU), and tetrahydrofuran (THF) are similarly classified as hazardous and pose toxicological risks.[19] To enable the sustainable commercialization of perovskite technologies, early-stage efforts must prioritize the development of eco-friendly solvent systems and implement rigorous handling protocols to mitigate health and ecological impacts without compromising device performance. Vidal et al.[19] conducted a comprehensive analysis of the environmental and health impacts of eight solvents—DMF, DMSO, DMAC, NMP, GBL, THF, and DMPU—commonly used in perovskite processing. The study evaluated the full life cycle of these solvents, considering factors like production, use, emissions, and end-of-life treatments, including incineration and recycling. They employed the USEtox model – a scientific tool for assessing potential toxicity to humans and ecosystems across a solvent's life cycle – and expanded the analysis to include broader toxicity data, encompassing not only carcinogenic risks but also other potential hazards.[19] DMSO emerged as the most sustainable choice among the solvents studied, offering the lowest combined environmental and human health impact.

Despite its promising environmental and health benefits, DMSO, used as a sole solvent, has not been widely adopted for perovskite film fabrication, primarily due to its high viscosity and relatively slow evaporation rate compared to other commonly used solvents, such as DMF.[25–27] These properties can complicate the film-forming process, leading to challenges in achieving the optimal film morphology and homogeneity required for high-performance perovskite devices.[28] Additionally, DMSO's higher boiling point can necessitate more rigorous processing conditions or longer annealing times, increasing energy consumption and production costs. Several studies have attempted to overcome these challenges by exploring DMSO in combination with other solvents or optimizing processing techniques. For instance, a study by Yang et al.[29] demonstrated the use of DMSO in a mixed solvent system, which successfully produced high-quality perovskite films with improved morphology and performance. Similarly, Li et al.[30] investigated the use of DMSO in conjunction with hydrochloric acid to enhance the film's crystallinity and device efficiency, achieving an impressive PCE. However, these studies highlighted that while DMSO offers superior environmental and health benefits, it still requires additional optimization to compete with more commonly used solvents, such as DMF and DMSO mixtures, in terms of ease of processing and device performance. This suggests that its full potential in perovskite photovoltaics will only be realized

through continued refinement of processing techniques and solvent formulations.

In the same vein, anti-solvents are crucial in perovskite solar cell fabrication as they enhance film quality by promoting rapid crystallization, improving morphology, and controlling grain growth.[31] Common anti-solvents, such as chlorobenzene, toluene, and diethyl ether, are effective in these processes but pose significant environmental and health risks. Chlorobenzene and toluene are toxic, with potential carcinogenic effects, while diethyl ether is highly flammable, raising concerns about worker safety and environmental impact. Isopropanol (IPA) and ethanol (EtOH) offer safer alternatives. Both are less toxic, biodegradable, and have lower flammability risks than traditional anti-solvents. Studies have shown that both IPA and EtOH can be used to achieve high-quality perovskite films with similar or even improved photovoltaic performance compared to conventional anti-solvents, thus supporting the transition to more environmentally friendly and sustainable fabrication methods,[31–33] in combination with DMSO. By adopting IPA and EtOH, the perovskite solar industry can reduce health risks and environmental impact while maintaining the high efficiency necessary for commercial viability.[31] These safer solvents align with the ongoing shift toward more sustainable manufacturing practices in the renewable energy sector.

Recent years have seen notable strides in developing eco-friendly solvent strategies for perovskite precursor inks, incorporating lactones, alcohols, water-based systems, and other sustainable alternatives. γ-Valerolactone (GVL) and ethyl lactate, both biodegradable lactones, have demonstrated high precursor solubility and enabled stable large-area devices with PCEs above 13%.[34,35] Alcohols such as EtOH and IPA have been explored not only as safer anti-solvents but also as co-solvents to reduce toxicity while preserving film quality.[36] Beyond these, ionic liquids and deep eutectic solvents have emerged as low-volatility, recyclable media that enhance crystallinity and improve device stability under humid conditions.[37,38] More recently, attempts have been made to exploit water as an eco-friendly solvent – for instance, aqueous lead nitrate or lead acetate solutions combined with hydrophilic additives and controlled crystallization routes have produced stable films and devices, underscoring the possibility of integrating water into perovskite processing despite its inherent challenges.[24,39] Together, these advances underscore the growing feasibility of sustainable solvent systems that balance environmental safety with the efficiency demands of next-generation MHP-PVs.

In this study, we explored the potential of DMSO as a sole solvent for processing $(FA)_{0.77}(MA)_{0.23}Pb(I)_{2.74}(Cl)_{0.26}$ perovskite material under ambient conditions. We also demonstrated the effectiveness of IPA or EtOH, in combination with DMSO, as solvents for the simple spin-coating processing of perovskite thin films. The DMSO-IPA system enables the fabrication of semitransparent perovskite solar cells that achieved a PCE of 12.0%, with a thin-film average visible transmittance (AVT) of 39.1% and a light utilization efficiency (LUE) of about 4.69%. Additionally, considering the photopic response of the human eye – a key factor for applications in transparent building-

integrated photovoltaics (BIPV) – an average photopic transmittance (APT) of 27.9% was obtained, corresponding to a LUE of 3.34%. To enhance optical transparency, the gold electrode thickness was reduced from 80 nm to 30 nm, leading to increased device-level AVT and APT values. Interestingly, while thin-film data initially suggested comparable/lower LUEs for 30 nm of gold devices, full-device transmittance measurements revealed a more realistic picture: the DMSO IPA 5K device with 30 nm of gold achieved a true LUE of 0.59% and 0.88% (using AVT and APT values, respectively), compared to just 0.03% (using AVT value) and 0.033% (using APT value) for its 80 nm counterpart. This underscores the limitations of relying solely on thin-film transmittance and highlights the necessity of complete device optical characterization for accurate evaluation of semitransparent performance. These results demonstrate the feasibility of fabricating high-performance semitransparent solar cells under ambient conditions. This reduces reliance on sophisticated controlled environments, thereby advancing the feasibility of scaling this technology for real-world applications. Future studies will explore the integration of fully transparent or semitransparent conductive electrodes to further optimize LUE in these devices. For BIPV applications, further research may be needed to address the color issues associated with the color rendering index while maintaining a good level of APT and PCE. We believe this can be achieved by tuning the perovskite composition to obtain a reasonable optical bandgap, which could be a limiting factor.

2. Experimental section

2.1. Materials and solution preparation

The precursor materials were procured from GreatCell Solar Materials and TCI Chemicals, while solvents were sourced from Sigma-Aldrich. For the preparation of the $FA_{0.77}MA_{0.23}$-$PbI_{2.77}Cl_{0.23}$ perovskite solution, we used a modified recipe reported by Cho et al.[40] The precursors formamidinium iodide (FAI, 1.6 M), lead(II) iodide (PbI_2, 1.6 M), and methylammonium chloride (MACl, 0.48 M) were dissolved in 1 mL of a DMF:DMSO solvent mixture (with a 14% vol ratio of DMSO), serving as the reference solution. For a greener processing of the perovskite ink, the same FAI, PbI_2, and MACl concentrations were dissolved in 1 mL of pure DMSO. The solutions were stirred at 50 °C for 2 to 4 hours in ambient conditions.

The electron transport layer (ETL) solution was prepared by diluting tin(IV) oxide (SnO_2) nanoparticles (obtained from Alfa-Aesar) in deionized water at a 1:7 volume ratio, ensuring uniform nanoparticle dispersion for optimal thin-film quality. A potassium chloride (KCl) buffer solution was prepared by dissolving 10 mg of KCl in 3 mL of deionized water and stirring at room temperature. The hole transport layer (HTL) solution was prepared by dissolving 72.3 mg of spiro-OMeTAD in 1 mL of chlorobenzene, followed by the sequential addition of 28.8 μL of 4-tert-butylpyridine and 17.5 μL of a bis(trifluoromethane)-sulfonimide lithium salt (Li-TFSI, 520 mg mL^{-1}) solution in acetonitrile as dopants. Furthermore, an additional 29 μL of

cobalt(II)-TFSI (FK209, 300 mg mL^{-1}) dopant solution in acetonitrile was incorporated. These additives are crucial for enhancing ionic conductivity, improving charge transport, and stabilizing the HTL, thereby contributing to the overall performance of perovskite solar cells.

2.2. Device fabrication

Indium tin oxide (ITO)-coated glass substrates with sheet resistance between 12–20 Ω sq^{-1}, supplied by Colorado Concept Coating LLC, were cleaned in a multistep protocol via ultrasonication for 15 minutes each in Hellmanex III detergent-deionized water, deionized water, acetone, and IPA. The substrates were subsequently dried, preheated in an oven at 120 °C for 20 minutes, and UV-Ozone-treated for 20 minutes.

The electron transport layer (ETL) of SnO_2 was spin-coated at 3000 rpm for 30 seconds, followed by annealing at 150 °C for 30 minutes, followed by a potassium chloride (KCl) buffer layer, deposited by spin-coating at 5000 rpm for 20 seconds, with subsequent annealing at 100 °C for 20 minutes. The deposition of the perovskite layers was achieved using a two-step spin-coating technique. During the first step, the films were spun at 2000 rpm for 20 seconds, followed by a second step at 5000 rpm for another 20 seconds. To regulate the crystallization process and improve the film uniformity, IPA or EtOH anti-solvent (0.2 mL) was dripped onto the spinning films 10 seconds before the end of the second spin cycle. The perovskite thin film was annealed at 150 °C for 10 minutes. Films prepared with the DMF:DMSO solution and treated with IPA at the initial spin speed of 2000 rpm were designated as DMF:DMSO IPA 2K, while their DMSO-only counterparts were labeled DMSO IPA 2K. Similarly, those treated with EtOH under identical conditions were referred to as DMF:DMSO EtOH 2K and DMSO EtOH 2K, respectively.

Following this, 50 μL of the spiro-OMeTAD hole transport layer (HTL) solution was spin-coated at 3000 rpm for 30 seconds. The devices were then left overnight to facilitate the oxidation of spiro-OMeTAD. Finally, 80 nm (for opaque devices) and 30 nm (for semitransparent devices) of gold electrodes were thermally evaporated through a shadow mask under a vacuum of 1.2 × 10^{-6} mbar, precisely defining the active device area (0.092 cm^2) of the device. For accurate thickness control, we used a thermal evaporator that was optimized by measuring the deposited gold thickness using an optical profilometer. During the optimization, we repeated the depositions and recalculated the tolling factor of the evaporator until the measured thickness from the profilometer matched the reading from the evaporator screen for each type of device, i.e., the 80 nm device and the 30 nm device.

2.3. Characterization

The nanostructure morphology of the perovskite films was characterized by a field-emission scanning electron microscope (Verios G4 XHR SEM, Thermo Scientific), while the optical bandgap and transmittance were analyzed by UV-vis-NIR absorption spectroscopy using a PerkinElmer Lambda 1050 + Spectrometer with integrating spheres. The thickness and

roughness of the films were characterized using the Bruker DektakXT Stylus optical profilometer. For the X-ray diffraction (XRD) analysis, a Malvern Panalytical Empyrean IV equipped with a PIXcel 3D and 1Der detector was employed to assess the crystallinity and phase composition of the perovskite films. Time-resolved photoluminescence (TRPL) characteristics were obtained using an FLS1000 spectrometer from Edinburgh Instruments. Fourier transform infrared (FTIR) spectroscopy was performed in transmission geometry under nitrogen purge using a Bruker Vertex 70 spectrometer equipped with a liquid nitrogen-cooled mid-band mercury cadmium telluride (MCT) detector. A total of 500 scans were averaged at a resolution of $4~cm^{-1}$, and the absorbance was calculated by referencing the clean, bare substrate. The J–V characteristics were measured using the Newport solar simulator under simulated $100~mW~cm^{-2}$ AM 1.5 G solar radiation. The short-term photostability of the devices was conducted by recording their J–V response under constant illumination of $100~mW~cm^{-2}$ using a steady-state LED lamp (Ossila Solar Simulator Class AAA).

3. Results and discussion

3.1. Thin film characteristics

Two distinct perovskite precursor solutions were prepared: a mixed-solvent system comprising toxic *N,N*-dimethylformamide (DMF) and dimethyl sulfoxide (DMSO), labeled as DMF:DMSO, and a single-solvent system utilizing DMSO exclusively, referred to as DMSO, which offers a more eco-friendly alternative. They were deposited as the active layer in the device architecture depicted in Fig. 1(a). Fig. 1a also shows the eco-friendly anti-solvent treatment with IPA and EtOH, with all layers between the ITO substrates and Au processed under ambient conditions. To reduce the active layer thin film thickness and enhance semitransparency, the spin speed of the first step in the spin-coating protocol was increased to 5000 rpm, while keeping the second step at 5000 rpm. The thin films produced under these modified conditions were designated as DMF:DMSO IPA 5K or DMSO IPA 5K for IPA-treated films and DMF:DMSO EtOH 5K or DMSO EtOH 5K for EtOH-treated films.

Fig. 1(b) presents photographs of the fabricated device stack before the deposition of the gold counter electrodes, highlighting the visual differences between the various perovskite films. The blue box depicts the top view from the spiro-OMeTAD hole transport layer, while the red box provides a view of the stack from the glass substrate. Notably, the devices fabricated using the DMF:DMSO solution, specifically DMF:DMSO IPA 2K and DMF:DMSO IPA 5K, exhibit a uniform, opaque appearance with no observable semitransparency. This lack of transparency can be attributed to the high viscosity and rapid crystallization dynamics facilitated by the toxic DMF:DMSO solvent mixture.[41] In contrast, the devices processed using the eco-friendly DMSO-only solvent, DMSO IPA 2K and DMSO IPA 5K, exhibit a significant degree of semitransparency, with the latter (DMSO IPA 5K) achieving the highest transparency. This distinction is particularly evident in the photograph, where the logo beneath the substrate remains legible through the perovskite layer in DMSO IPA 5K. The superior transparency in these devices is likely due to the slower crystallization dynamics of the DMSO solvent, which facilitates more uniform film thinning at higher spin-coating speeds.[41] This stark difference in film transparency not only underscores the impact of solvent choice on the optical properties of the perovskite films but also highlights the feasibility of using DMSO as a safer alternative for achieving semitransparent devices suitable for possible applications in agrivoltaics or BIPVs.

The optical properties of the perovskite thin films deposited on ITO-coated glass substrates were investigated using UV-vis-NIR spectroscopy. Fig. S1(a) in the SI illustrates the Tauc plots derived from the absorption data through the application of the Tauc equation, which establishes the relationship between the absorption coefficient (α) and the incident photon energy ($h\nu$):[42,43]

$$(\alpha h\nu) = A(h\nu - E_g)^n \tag{1}$$

where α represents the absorption coefficient, $h\nu$ denotes the incident photon energy, A is a proportionality constant, E_g signifies the bandgap energy, and n corresponds to the electronic transition type, taking a value of 2 for direct bandgap materials and 1/2 for indirect bandgap materials.
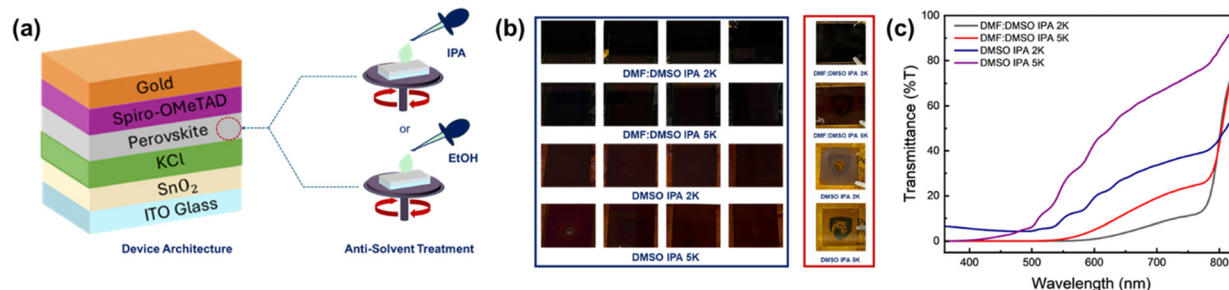

Fig. 1 (a) Device architecture and eco-friendly anti-solvent treatment process. (b) Natural photographs of the device stack with all other layers except gold, with a blue box showing the top view from the spiro-OMeTAD layer and a red box showing the back view from the glass side, with a logo underneath to determine semitransparency. (c) Transmittance of IPA-treated perovskite thin films using a UV-vis-NIR spectrometer with an integrating sphere.

Given that the perovskite material under study exhibits a direct bandgap, $n = 2$ was employed. The Tauc plots reveal that the bandgap of the films remained consistent at approximately $E_g \sim 1.50$ eV, irrespective of variations in the solvent system or spin-coating parameters. This observation is corroborated by similar trends in EtOH-treated samples, as shown in Fig. S1(b) of the SI. The consistency of the bandgap aligns with expectations since alterations in the solvent system and processing parameters should not affect the chemical composition of the perovskite. Fig. 1(c) presents the transmittance spectra of the samples in the visible and near-infrared regions. The DMF:DMSO IPA 2K sample exhibited the lowest transmittance ($\sim 30\%$), with light transmission visibly and highly reduced up to 770 nm. While a slight improvement (from 500 to 770 nm) was observed with the DMF:DMSO IPA 5K thin film, the overall transmittance and the cut-off wavelength remained comparable to that of DMF:DMSO IPA 2K. In contrast, thin films fabricated with the eco-friendly DMSO-only solvent demonstrated a significant enhancement in transmittance value over a broader spectral range. Notably, the DMSO IPA 5K thin film exhibited the highest transmittance, surpassing 75% at longer wavelengths and maintaining reduced but reasonable transmission up to 400 nm. This trend correlates strongly with the visual observations in Fig. 1(b) and is further substantiated by the thickness measurements shown in Fig. S2(a). The average thicknesses of DMF:DMSO IPA 2K, DMF:DMSO IPA 5K, DMSO IPA 2K, and DMSO IPA 5K were determined to be 744 ± 72 nm, 485 ± 21 nm, 169 ± 17 nm, and 132 ± 13 nm, respectively. Similar trends were observed for EtOH-treated samples, as depicted in Fig. S1(c) and S2(b) in the SI, although the transmittance values were slightly lower than those of their IPA-treated counterparts. This slight deviation might be attributed to the higher polarity of ethanol, which can lead to slightly altered film morphology and surface roughness, thereby affecting light transmission.[44]

To quantify the optical performance of the perovskite thin films, the average visible transmittance (AVT) and average photopic transmittance (APT) were calculated based on the transmittance spectra. These metrics are useful for evaluating light transmission properties in specific spectral ranges and under varying visual and photopic conditions. The AVT was determined using eqn 1 in the SI. In contrast, the APT, by weighting transmittance against human photopic sensitivity, provides insights into how effectively a material transmits light in a manner that aligns with human vision, making it more relevant for optoelectronic and architectural glazing applications.[8] This was determined using the following equation:[45]

$$\text{APT} = \frac{\int_{360}^{830} T(\lambda) P(\lambda) s(\lambda) \mathrm{d}\lambda}{\int_{360}^{830} P(\lambda) s(\lambda) \mathrm{d}\lambda} \qquad (2)$$

In this equation, $P(\lambda)$ denotes the photopic response function, and $s(\lambda)$ represents the light source spectral distribution. This weighted metric better reflects how the human eye perceives transmittance under daylight or artificial lighting conditions.

Table 1 Comparison of semitransparent and optoelectronic properties of IPA-treated thin films and devices

Device type	AVT (%)	APT (%)	PCE (%)	LUE using AVT (%)	LUE using APT (%)
Thin Films Transmittance/Devices with 30 nm of Gold Electrode					
DMF:DMSO IPA 2K	8.5	0.6	14.7	1.25	0.09
DMF:DMSO IPA 5K	12.6	2.6	13.9	1.75	0.36
DMSO IPA 2K	20.9	12.1	11.4	2.38	1.37
DMSO IPA 5K	39.1	27.9	10.9	4.26	3.04
Full device transmittance/devices with 30 nm of gold electrode					
DMF:DMSO IPA 2K	0.89	0.29	14.7	0.13	0.04
DMF:DMSO IPA 5K	2.50	2.64	13.9	0.35	0.37
DMSO IPA 2K	4.71	5.90	11.4	0.54	0.67
DMSO IPA 5K	5.40	8.08	10.9	0.59	0.88

The AVT and APT values (in Table 1) show a clear trend of increasing transmittance as the solvent system transitions from DMF:DMSO to DMSO-only and as the spin-coating speed increases. Notably, the DMSO IPA 5K sample exhibits the highest AVT and APT values (39.1% and 27.9%, respectively), reflecting its superior light transmission properties. In contrast, the DMF:DMSO IPA 2K sample demonstrates the lowest AVT and APT values (8.5% and 0.6%, respectively). This is consistent with its lower visual transmittance and thicker film morphology, as discussed earlier. This trend supports the idea that the solvent system and film thickness have a significant influence on the optical properties. For EtOH-treated samples, the AVT and APT values (Table S5) follow a similar increasing trend but are generally lower than those of the IPA-treated counterparts.

To investigate the morphology of the perovskite thin films on ITO-glass substrates, field emission scanning electron microscopy (FE-SEM) was employed in immersion mode. Fig. 2(a and d) illustrates the SEM images of the IPA-treated samples, while Fig. S6(a) in the SI shows the grain size distributions derived from the same images. The roughness values of these samples are presented in Fig. S2(c) in the SI. The DMF:DMSO IPA 2K sample (Fig. 2(a)) displays the largest, compact grains with no visible pinholes or excess PbI_2. The average grain size is 1.1 μm, as shown in Fig. S6(a) of the SI, with an average roughness value of 23.3 nm. This morphology aligns with its high film thickness and lower transmittance, indicative of denser films. The DMF:DMSO IPA 5K sample (Fig. 2(b)) shows similarly large and compact grains with some PbI_2 evident at the grain boundaries. This PbI_2 can act as a passivation agent, potentially improving the optoelectronic properties of the film.[46,47] The grain size of 0.90 μm is slightly smaller than that of the DMF:DMSO IPA 2K samples, and the average roughness decreases to 11.1 nm, indicating a smoother surface. Conversely, the DMSO-IPA samples exhibit smaller grain sizes. The DMSO IPA 2K sample (Fig. 2(c)) exhibits significantly reduced grains of 0.40 μm and regions of excess PbI_2. Additionally, the average roughness value of 18.9 nm suggests uniform film coverage with incomplete PbI_2 conversion, explaining its higher transmittance and reduced thickness compared to its DMF:DMSO counterpart. The DMSO IPA 5K sample (Fig. 2(d)) shares a similar grain size (0.40 μm) with the DMSO IPA 2K sample but exhibits a more uniform morphology, with no pinholes and a substantially lower roughness value of 2.2 nm. This smoother surface could be
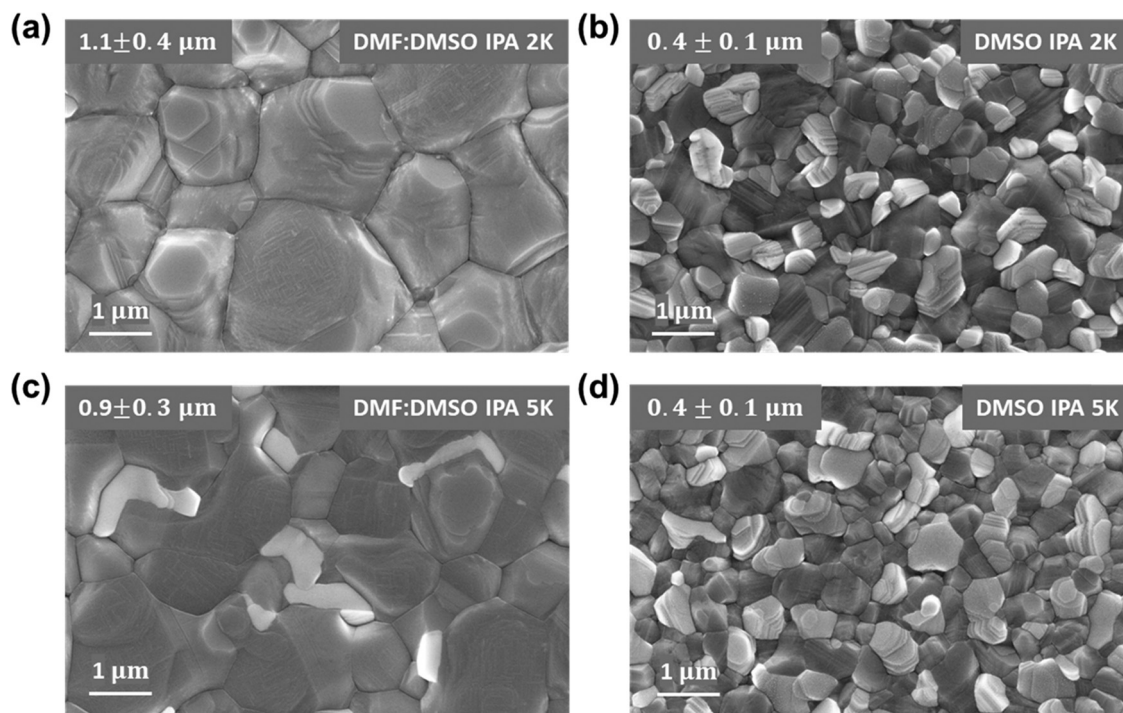
Paper

Fig. 2 SEM images of IPA-treated perovskite thin films: processed from DMF:DMSO (a) 2000 rpm (2K) and (b) 5000 rpm (5K); and processed from DMSO (c) 2000 rpm (2K) and (d) 5000 rpm (5K). The average grain size distribution is indicated on the top-left of each micrograph.

advantageous for applications requiring high transparency and uniformity, correlating with the highest transmittance and low thickness of its thin films.

Fig. S5(a–d) in the SI provides a comparable analysis for EtOH-treated samples. Although similar trends are observed, notable differences are also present. For instance, the average grain sizes of the DMF:DMSO EtOH-treated samples are slightly larger, and PbI$_2$ is visible at the grain boundaries of both DMF:DMSO EtOH 2K and DMF:DMSO EtOH 5K. This contrasts with the IPA-treated samples, where excess PbI$_2$ is primarily observed at higher spin speeds. Furthermore, the DMSO EtOH 5K sample retains pinholes, unlike its IPA-treated counterpart, despite having similar grain sizes. Overall, the roughness values show a general decrease with increased spin speed for both solvent systems, with DMSO-based films exhibiting comparatively lower roughness values. These findings complement the earlier optical and thickness measurements, reinforcing the relationship between solvent choice, processing conditions, and the resulting film morphology.

To investigate the crystallinity and phase composition of the perovskite thin films, X-ray diffraction (XRD) was performed on thin films deposited on ITO glass substrates. The XRD patterns of the IPA-treated films, presented in Fig. 3(a), exhibit the characteristic perovskite (001) and (002) diffraction peaks at approximately $2\theta = 13.4°$ and $27.6°$, respectively, as also shown in ref. 40. While the DMSO-based samples show a significant reduction in perovskite peak intensity and an increase in PbI$_2$ peaks (potentially due to the high concentration of PbI$_2$ in our perovskite composition and the limited solubility of PbI$_2$ in

DMSO), there are no additional peaks to suggest decomposition or the presence of an undesired secondary phase. A particularly interesting observation is the absence of the PbI$_2$ peak in the DMF:DMSO IPA 2K sample, whereas it appears in the DMF:DMSO IPA 5K counterpart. This trend aligns with the SEM images in Fig. 2(a) and (b), where excess PbI$_2$ was observed at grain boundaries in the latter sample. The presence of PbI$_2$ in moderate amounts could indicate partial passivation effects, which may be beneficial for device performance. In contrast, excessive PbI$_2$ may suggest incomplete conversion to the perovskite phase, possibly due to the strong coordination of DMSO with Pb^{2+}, which stabilizes PbI$_2$.DMSO intermediate phase.[46–48] Additionally, in the XRD patterns, films processed from pure DMSO exhibit relatively higher residual PbI$_2$ signals compared to those obtained from DMF:DMSO mixtures. This observation is closely related to the reduced thickness and increased transparency of DMSO-derived films. Since XRD peak intensities scale with the volume of crystalline material sampled within the penetration depth, thinner absorbers yield weaker perovskite reflections, thereby amplifying the relative contribution of PbI$_2$ peaks. The corresponding optical data corroborates this trend: DMSO-only films show higher average visible transmittance (AVT), consistent with their reduced thickness and lower optical density. Interestingly, ITO substrate signals are not observed in the diffractograms, which can be attributed to attenuation of the substrate scattering by the perovskite layers, the inherently broad and weak diffraction features of polycrystalline ITO, peak overlap with stronger perovskite reflections, and/or the limited penetration depth of the XRD tool. For the
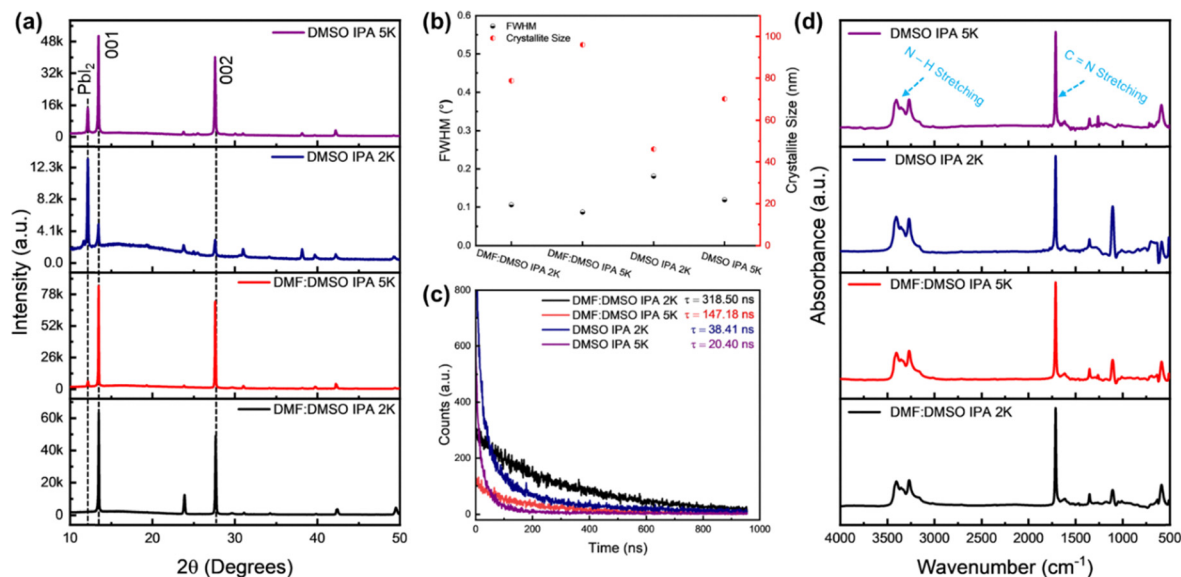
Fig. 3 (a) XRD pattern of IPA-treated perovskite thin films. (b) The full width at half maximum (FWHM) and crystallite sizes of IPA-treated perovskite thin films. (c) Time-resolved photoluminescence (TRPL) of IPA-treated perovskite thin films on ITO/SnO$_2$ substrates. (d) FTIR Spectra of the DMF:DMSO-based and DMSO-based IPA-treated thin films after annealing.

EtOH-treated samples, the XRD patterns in Fig. S7(a) reveal similar trends but with key differences. Notably, PbI$_2$ peaks appear in all EtOH-based films, and the (001) and (002) perovskite peaks of the DMSO-only films are weak, suggesting that the perovskite phase is less stable in DMSO EtOH-treated films compared to their DMSO IPA-treated counterparts. Interestingly, in contrast to the IPA-treated samples, the PbI$_2$ peak is more pronounced in the DMF:DMSO EtOH 2K sample than in DMF:DMSO EtOH 5K, where it is nearly absent. This trend may be due to the higher polarity of ethanol, which alters intermediate phase formation and crystallization kinetics differently than IPA.[49]

To further assess crystalline quality, Fig. 3(b) presents the full width at half maximum (FWHM) and crystallite sizes of the IPA-treated samples, obtained using Scherrer's equation:[1]

$$D = K\frac{\lambda}{\beta \cos\theta} \tag{3}$$

where D is the crystallite size, λ = 0.154 nm is the X-ray wavelength, K = 0.9 is the Scherrer constant, β is the FWHM of the (001) peak, and θ is the corresponding diffraction angle. The results indicate that the crystallite sizes of DMF:DMSO-based and DMSO-based samples increase with speed, even though those of the DMSO-based films are lower than those of their DMF:DMSO-based counterparts. This trend is mirrored in the FWHM values, where DMSO IPA 2K exhibits the highest FWHM, indicating a smaller crystallite size and potentially increased microstrain.[40] These findings reinforce the trends observed in SEM and optical transmittance analyses. Interestingly, despite their lower crystallinity and smaller crystallite sizes, the DMSO-based films exhibit higher transmittance and greater semitransparency compared to DMF:DMSO-based films. This is likely due to reduced light scattering from smaller

grains.[50] For the EtOH-treated samples, determining the crystallite size was more challenging due to the weaker peak intensities, particularly in the DMSO-based films. This further supports the observation that ethanol processing leads to reduced crystallinity, likely due to altered nucleation and growth mechanisms.

To investigate charge carrier recombination and transport in our perovskite thin films, we performed time-resolved photoluminescence (TRPL) measurements on samples deposited on ITO/SnO$_2$ substrates. Fig. 3(c) presents the TRPL spectra of the DMF:DMSO- and DMSO-based IPA-treated samples. A biexponential fitting approach was employed to extract the charge carrier lifetimes, summarized in Table S1. The slow decay regime (τ_1) is typically attributed to defect-mediated nonradiative recombination at grain boundaries, while the fast decay regime (τ_2) corresponds to charge carrier quenching at the perovskite/substrate interface and within the bulk. The average lifetimes (τ) were found to be 318.5 ns, 147.2 ns, 38.4 ns, and 20.4 ns for DMF:DMSO IPA 2K, DMF:DMSO IPA 5K, DMSO IPA 2K, and DMSO IPA 5K, respectively, consistent with the trends in crystallinity and morphology observed in the SEM and XRD analyses.

To ensure phase purity and verify the absence of intermediate phases, we conducted Fourier-transform infrared spectroscopy (FTIR) on perovskite thin films deposited on silicon substrates. The FTIR spectra, shown in Fig. 3(d), reveal nearly identical absorption features across all samples, confirming consistent perovskite phase formation irrespective of the solvent system. The characteristic vibrational bands for FA$^+$ (C=N stretching at approximately 1716 cm^{-1}) and MA$^+$ (N–H stretching at approximately 3276 cm^{-1}) are present in all cases, indicating successful incorporation of both cations in the final perovskite structure. In addition to the annealed films, we also

characterized fresh, unannealed films on silicon substrates (see Fig. S7(b) in the SI). These spectra exhibited additional absorption peaks around 1000 cm^{-1}, attributed to the presence of DMSO solvent residues in the as-deposited perovskite precursor films. Despite these additional features, the characteristic perovskite vibrational peaks remained present in the unannealed samples, indicating that the fundamental phase already begins to form even before thermal treatment. These results confirm that all solvent systems yield perovskite films with comparable final compositions after annealing, while highlighting the importance of the annealing step for removing residual solvents. This finding underscores the crucial role of solvent engineering in ambient-processed perovskite solar cells. While different solvent systems affect film microstructure, charge recombination dynamics, and optical transparency, the overall phase composition remains stable.

3.2. Device characteristics

To evaluate the photovoltaic performance of the perovskite films, we fabricated solar cells using the ITO/SnO$_2$/KCl/Perovskite/Spiro-OMeTAD/Au architecture, as shown in Fig. 1(a) and detailed in the experimental section. The J–V curves of the best-performing devices, fabricated using IPA-treated perovskite thin films with an 80 nm gold top electrode, are presented in Fig. S8(a) in the SI. These measurements were conducted under 1 sun (AM 1.5G) illumination, and the corresponding device parameters – power conversion efficiency (PCE), short-circuit current density (J_{SC}), open-circuit voltage (V_{OC}), and fill factor (FF) – are summarized in Table S2 in the SI. The results indicate that DMF:DMSO-based devices outperform their DMSO-only counterparts in terms of efficiency. The highest PCE achieved is 21.3% for DMF:DMSO IPA 2K, followed by 19.8% for DMF:DMSO IPA 5K. In contrast, the DMSO-based devices exhibit lower efficiencies, with DMSO IPA 2K and DMSO IPA 5K achieving 14.7% and 12.0%, respectively. A noticeable decline in PCE is observed as the spin speed increases from 2K to 5K, likely due to a corresponding reduction in film thickness, as corroborated by the thickness measurements in Fig. S2(a) in the SI. The statistical analysis of the J–V parameters, presented in Fig. S8(b–e) in the SI, demonstrates high reproducibility across multiple device sets, confirming the observed trend: a decrease in efficiency as we transition from DMF:DMSO IPA 2K to DMSO IPA 5K. This variation in performance is closely linked to the morphological and structural properties observed in previous characterizations. The XRD and SEM analyses indicate that DMF:DMSO-based perovskites exhibit superior crystallinity and reduced defect density, contributing to their higher efficiency. A similar trend is observed in EtOH-treated perovskite devices, as detailed in Fig. S9 and Table S4 in the SI. However, these devices show greater variability, primarily due to performance degradation at relative humidity (RH) levels below 30%. The best-performing EtOH-treated devices achieve PCE values of 19.2% (DMF:DMSO EtOH 2K), 17.2% (DMF:DMSO EtOH 5K), 17.5% (DMSO EtOH 2K), and 7.4% (DMSO EtOH 5K). Notably, the severe efficiency drop in DMSO EtOH 5K and the difficulty in reproducing its

performance highlight the limitations of EtOH as an anti-solvent, reinforcing IPA as a more reliable alternative for perovskite processing.

While PCE remains a crucial metric, this study emphasizes semitransparency and environmental sustainability. To quantify the trade-off between transparency and efficiency, we calculated the light utilization efficiency (LUE) using the AVT and APT values discussed earlier (derived from Fig. S10(a–d)), alongside the PCE values obtained here. As presented in Table 1 and Table S5 in the SI, the LUE increases as we transition from DMF:DMSO IPA 2K to DMSO IPA 5K, demonstrating that DMSO-based devices, despite their lower efficiency, provide a superior transparency-performance balance. This observation is further confirmed by the external quantum efficiency against wavelength measurement shown in Fig. S11 in the SI, which demonstrates that DMSO-based devices exhibit a decrease in EQE in the visible wavelength range due to increased transmittance or semitransparency. Using AVT-based calculations, the LUE values (based on the efficiencies of the 80 nm gold device using AVT of the films) are 1.81% for DMF:DMSO IPA 2K, 2.50% for DMF:DMSO IPA 5K, 3.07% for DMSO IPA 2K, and 4.69% for DMSO IPA 5K. Similarly, using APT-based calculations, the LUE values are 0.12%, 0.51%, 1.77%, and 3.34%, respectively. This trend is also observed in EtOH-treated devices, but their LUE values are comparatively lower, consistent with the variations in their J–V parameters (Table S5 in the SI).

An essential consideration for semitransparent solar cells is the transparency of the top electrode. Since our device architecture utilizes gold, an opaque metal, achieving semitransparency requires reducing the electrode thickness. To this end, we decreased the gold thickness from 80 nm to 30 nm, enhancing the transparency of the entire device. The transparency of the fabricated solar cells is shown in Fig. S10(f) of the SI, where the blue box highlights all the devices, and the red box emphasizes the improved semitransparency of the DMSO-based devices, as evident from the visibility of the underlying text through the device structure. Fig. 4(a) presents the J–V characteristics of the best-performing devices with 30 nm of gold, measured under 1 sun (AM 1.5G) illumination. The corresponding device metrics are summarized in Table S3 in the SI. The same performance trends observed for the 80 nm gold devices persist here, with a key distinction: a reduction in PCE across all devices. This decrease is primarily attributable to contact resistance issues arising from the reduced gold thickness, which diminishes charge extraction efficiency. The PCE values for DMF:DMSO IPA 2K, DMF:DMSO IPA 5K, DMSO IPA 2K, and DMSO IPA 5K are 14.7%, 13.9%, 11.4%, and 10.9%, respectively. A closer examination of the figures of merit reveals that the fill factor (FF) is the parameter most significantly affected by the gold thickness reduction. For the 30 nm gold devices, the FF values are 68.2% for DMF:DMSO IPA 2K, 71.8% for DMF:DMSO IPA 5K, 61.2% for DMSO IPA 2K, and 59.5% for DMSO IPA 5K. In contrast, for the 80 nm gold devices, the FF values were 75.3%, 77.3%, 74.5%, and 63.3% for the same set of samples, respectively. This substantial FF reduction, especially in the
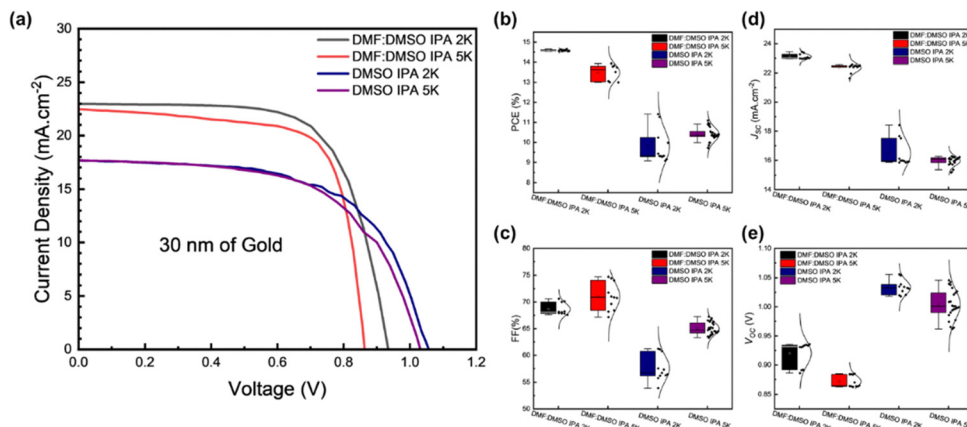
Fig. 4 (a) The J–V curves of the IPA-treated fabricated solar cell devices containing 30 nm of gold measured under 1 sun illumination. The statistical distribution of the different J–V parameters: PCE (b), FF (c), J_{SC} (d), and V_{OC} (e), respectively.

DMSO-based devices, suggests that the thinner gold layer introduces higher series resistance and lower conductivity, leading to inefficient charge collection. Interestingly, the short-circuit current density (J_{SC}) and open-circuit voltage (V_{OC}) remain largely unchanged between the 80 nm and 30 nm gold devices, with minor improvements in some instances. The consistency of J_{SC} values suggests that photon absorption and charge generation remain unaffected by electrode thickness. However, the statistical distribution plots of device performance metrics, shown in Fig. 4(b–e), reveal an unexpected trend in V_{OC}: on average, the V_{OC} values of the DMSO-based devices exceed those of the DMF:DMSO-based devices. This observation is likely due to differences in charge recombination dynamics, as the increased semitransparency of the DMSO-based devices may alter the interface properties, reducing recombination losses and slightly improving V_{OC}. For all devices, the LUEs were calculated as mostly recorded in the literature,[51–54] using the AVT and APT values derived from the thin film transmittance measurements. Although a reduction in PCE was observed due to the thinner electrode for the 30 nm electrode devices, the overall LUE trends mirrored those of the 80 nm devices, as shown in Table 1. For instance, the 30 nm electrode DMSO IPA 5K devices exhibit LUE values of 4.26% (using AVT) and 3.04% (using APT) compared to 4.69% and 3.34%, respectively, for their 80 nm electrode device counterparts. However, for a robust/honest evaluation, it is imperative to measure the transmittance of the complete device architecture, as this captures the cumulative effects of multi-layer interference, scattering, and absorption within the operational stack. Thus, it is intuitive to expect that devices with a 30 nm gold electrode would exhibit higher LUEs than their 80 nm counterparts, as a reduction in metallic thickness generally enhances optical transparency. Fig. S10(c) and S10(d) in the SI present the transmittance spectra of IPA-treated full devices with 80 nm and 30 nm gold electrodes, respectively. The calculated AVTs, APTs, and resulting LUEs (see Table 1) align with intuitive expectations, confirming that thinner metallic electrodes enhance the semitransparent

characteristics of the devices. The 30 nm electrode full device stack of DMSO IPA 5K exhibits LUE values of 0.59% and 0.88% (using AVT and APT) compared to 0.03% and a little over 0.03%, respectively, for the 80 nm electrode devices. This observation is consistent with the findings of Axelevitch et al.,[55] whose work (see Fig. S10(e) in the SI) demonstrated that decreasing the thickness of gold films increases their optical transmission. The discrepancy observed here highlights the inadequacy of thin-film transmittance measurements alone in accurately determining the AVT and APT of semitransparent devices. These insights emphasize the necessity of holistic device-level transmittance assessments when evaluating the semitransparent performance of perovskite solar cells.

Finally, short-term photostability measurements were performed in ambient conditions (20.8–21.5 °C temp; 38–44% RH) under open circuit conditions to ascertain the potential stability of the devices. The IPA-treated devices with 30 nm gold top electrodes demonstrate that the most semitransparent devices (DMSO IPA 5K) exhibit superior early stability compared to their DMF:DMSO counterparts, as illustrated in Fig. S12 of the SI. This improved photostability can be attributed to the inherent increase in semitransparency of the DMSO IPA 5K devices. This effectively allows most of the incident light to pass through the device, thereby reducing light absorption, especially compared to DMF:DMSO-based devices (cf. Fig. 1c). A primary driver of photo-induced degradation in perovskite solar cells is light absorption, as reported in the literature.[56–58] Additionally, the ability to maintain comparable performance in PCE despite the reduced gold thickness and an order of magnitude higher LUE values underscores the viability of semitransparent perovskite solar cells. Moreover, the superior transparency of the DMSO-based devices, combined with their eco-friendly processing, makes them particularly attractive for applications in building-integrated photovoltaics, agrivoltaics, and tandem solar cell configurations where light transmission is crucial. These findings further validate the importance of solvent selection in optimizing both efficiency and transparency in next-generation perovskite photovoltaics.

4. Conclusions

In summary, DMF:DMSO-based perovskites provide higher photovoltaic performance, while DMSO-only devices offer superior semitransparency, higher LUE, and eco-friendly processing, making them promising candidates for next-generation sustainable solar technologies. These results highlight simple methods and steps for fabricating an eco-friendly, semitransparent perovskite device, including the choice of green solvents, ambient processing, and thin film processing (spin coating) parameters, without adjusting the perovskite composition. The potential of coupling this simple green-solvent ambient process of semitransparent perovskite devices with the perovskite composition can be beneficial for advancing this technology. The practical advantages of DMSO-based devices, especially their higher LUE, make them ideal candidates for semitransparent photovoltaic applications. Given these characteristics, potential applications include: (i) building-integrated photovoltaics (BIPV) – the high light transmittance of DMSO-based devices makes them suitable for solar windows and facades, enabling energy generation while maintaining natural daylighting in architectural structures, (ii) agrivoltaics – their controlled transparency supports plant growth in solar greenhouses, allowing simultaneous electricity generation and sustainable farming, and (iii) self-powered electronics – DMSO-based semitransparent devices can be integrated into displays, smart windows, and wearable electronics, where maintaining aesthetics and visibility is essential.

Beyond performance, DMSO offers a significant environmental advantage over DMF, which is classified as a reproductive toxin. The use of DMSO as a benign solvent aligns with green chemistry principles, providing a more sustainable approach to fabricating perovskite solar cells. As the field advances toward scalable, eco-friendly perovskite technology, DMSO-based semitransparent solar cells offer a viable solution for integrating photovoltaics into a wider range of applications while minimizing environmental impact.

Author contributions

Cyril C. F. Kumachang: data curation, investigation, methodology, supervision, formal analysis, writing – original draft, and writing – review & editing; Brittlee G. Reese: data curation, investigation, formal analysis, and validation; Tawanda J. Zimudzi: data curation, formal analysis and writing – review & editing; Ivy M. Asuo: investigation, methodology, formal analysis, visualization, supervision, and writing – review & editing; and Nutifafa Y. Doumon: conceptualization, data curation, formal analysis, investigation, methodology, project administration, supervision, validation, visualization, writing – original draft, and writing – review & editing.

Conflicts of interest

The authors declare no conflict of interest.

Data availability

The data supporting this article are included in the article and in the supplementary information (SI). The SI includes absorbance, transmittance, and reflectance of EtOH-treated and IPA-treated thin films/devices; thickness and roughness of EtOH-treated and IPA-treated thin films; photographs of thin films on glass showing the difference in semitransparency of DMF:DMSO-based thin films at different spin-coating speeds compared to that of DMSO-based thin films at 5K rpm; SEM micrograph and XRD spectra of the thin films; J–V characteristics, EQE, and PV parameters of the perovskite solar cells; and ambient short-term photostability of IPA-treated semitransparent perovskite solar cells with a 30 nm gold top electrodes. See DOI: **https://doi.org/10.1039/d5ya00195a**.

References

1 I. M. Asuo, A. M. Varposhti, E. D. Gomez and N. Y. Doumon, *J. Mater. Chem. C*, 2024, **12**, 7562–7571.

2 S. Bhattarai, A. Mhamdi, I. Hossain, Y. Raoui, R. Pandey, J. Madan, A. Bouazizi, M. Maiti, D. Gogoi and A. Sharma, *Micro Nanostruct.*, 2022, **172**, 207450.

3 S. Bello, A. Urwick, F. Bastianini, A. J. Nedoma and A. Dunbar, *Energy Rep.*, 2022, **8**, 89–106.

4 Y. Sun, L. Ge, L. Dai, C. Cho, J. Ferrer Orri, K. Ji, S. J. Zelewski, Y. Liu, A. J. Mirabelli, Y. Zhang, J.-Y. Huang, Y. Wang, K. Gong, M. C. Lai, L. Zhang, D. Yang, J. Lin, E. M. Tennyson, C. Ducati, S. D. Stranks, L.-S. Cui and N. C. Greenham, *Nature*, 2023, **615**, 830–835.

5 I. M. Asuo, D. Gedamu, I. Ka, L. F. Gerlein, F.-X. Fortier, A. Pignolet, S. G. Cloutier and R. Nechache, *Nano Energy*, 2018, **51**, 324–332.

6 I. M. Asuo, D. Banerjee, A. Pignolet, R. Nechache and S. G. Cloutier, *Phys. Status Solidi RRL*, 2021, **15**, 2000537.

7 Z. Guo, A. K. Jena and T. Miyasaka, *ACS Energy Lett.*, 2023, **8**, 90–95.

8 S. Y. Kim, N. Rayes, A. R. Kemanian, E. D. Gomez and N. Y. Doumon, *Energy Adv.*, 2025, **4**, 37–54.

9 Y. Chen, S. R. Smock, A. H. Flintgruber, F. A. Perras, R. L. Brutchey and A. J. Rossini, *J. Am. Chem. Soc.*, 2020, **142**, 6117–6127.

10 *Alisonpotter2, World-leading 27% perovskite cell efficiency record set by UNSW and Soochow University, with ACAP support*, https://www.acap.org.au/post/world-leading-27-perovskite-efficiency-record-achieved-by-unsw-and-soochow-university-with-acap-su, (accessed June 18, 2025).

11 Best Research-Cell Efficiency Chart | Photovoltaic Research | NREL, https://www.nrel.gov/pv/cell-efficiency, (accessed June 12, 2025).

12 M. Qi, L. Jin, H. Yao, Z. Xu, T. Cheng, Q. Chen, C. Zhu and Y. Bai, *Acta Phys.-Chim. Sin.*, 2025, **41**, 100088.

13 M. A. Green, E. D. Dunlop, M. Yoshita, N. Kopidakis, K. Bothe, G. Siefer, X. Hao and J. Y. Jiang, *Prog. Photovoltaics Res. Appl.*, 2025, **33**, 795–810.

14 C. C. Boyd, R. Cheacharoen, T. Leijtens and M. D. McGehee, *Chem. Rev.*, 2019, **119**, 3418–3451.

15 S. Y. Kim, C. C. F. Kumachang and N. Y. Doumon, *Sol. RRL*, 2023, **7**, 2300155.

16 G. Schileo and G. Grancini, *J. Mater. Chem. C*, 2021, **9**, 67–76.

17 M. Yang, T. Tian, Y. Fang, W.-G. Li, G. Liu, W. Feng, M. Xu and W.-Q. Wu, *Nat. Sustainability*, 2023, **6**, 1455–1464.

18 S. K. Podapangi, F. Jafarzadeh, S. Mattiello, T. B. Korukonda, A. Singh, L. Beverina and T. M. Brown, *RSC Adv.*, 2023, **13**, 18165–18206.

19 R. Vidal, J.-A. Alberola-Borràs, S. N. Habisreutinger, J.-L. Gimeno-Molina, D. T. Moore, T. H. Schloemer, I. Mora-Seró, J. J. Berry and J. M. Luther, *Nat. Sustainability*, 2020, **4**, 277–285.

20 L. K. Ono, N.-G. Park, K. Zhu, W. Huang and Y. Qi, *ACS Energy Lett.*, 2017, **2**, 1749–1751.

21 R. Swartwout, M. T. Hoerantner and V. Bulović, *Energy Environ. Mater.*, 2019, **2**, 119–145.

22 Authorisation - ECHA, https://echa.europa.eu/substances-of-very-high-concern-identification-explained, (accessed November 22, 2024).

23 J. Sherwood, F. Albericio and B. G. De La Torre, *ChemSusChem*, 2024, **17**, e202301639.

24 M. T. Hoang, Y. Yang, N. D. Pham and H. Wang, *J. Phys. Chem. Lett.*, 2024, **15**, 6880–6889.

25 J. Wang, F. Di Giacomo, J. Brüls, H. Gorter, I. Katsouras, P. Groen, R. A. J. Janssen, R. Andriessen and Y. Galagan, *Sol. RRL*, 2017, **1**, 1700091.

26 Y. Galagan, F. Di Giacomo, H. Gorter, G. Kirchner, I. De Vries, R. Andriessen and P. Groen, *Adv. Energy Mater.*, 2018, **8**, 1801935.

27 O. Shargaieva, H. Näsström, J. A. Smith, D. Többens, R. Munir and E. Unger, *Mater. Adv.*, 2020, **1**, 3314–3321.

28 J. Küffner, J. Hanisch, T. Wahl, J. Zillner, E. Ahlswede and M. Powalla, *ACS Appl. Energy Mater.*, 2021, **4**, 11700–11710.

29 W. S. Yang, J. H. Noh, N. J. Jeon, Y. C. Kim, S. Ryu, J. Seo and S. I. Seok, *Science*, 2015, **348**, 1234–1237.

30 Y. Li, K. S. K. Lo and W. W.-F. Leung, *Sol. Energy*, 2017, **157**, 328–334.

31 A. D. Taylor, Q. Sun, K. P. Goetz, Q. An, T. Schramm, Y. Hofstetter, M. Litterst, F. Paulus and Y. Vaynzof, *Nat. Commun.*, 2021, **12**, 1878.

32 P. Mao, Q. Zhou, Z. Jin, H. Li and J. Wang, *ACS Appl. Mater. Interfaces*, 2016, **8**, 23837–23843.

33 Y. Wang, J. Wu, P. Zhang, D. Liu, T. Zhang, L. Ji, X. Gu, Z. David Chen and S. Li, *Nano Energy*, 2017, **39**, 616–625.

34 C. Worsley, D. Raptis, S. M. P. Meroni, R. Patidar, A. Pockett, T. Dunlop, S. J. Potts, R. Bolton, C. M. E. Charbonneau, M. Carnie, E. Jewell and T. Watson, *Mater. Adv.*, 2022, **3**, 1125–1138.

35 Y. Miao, M. Ren, Y. Chen, H. Wang, H. Chen, X. Liu, T. Wang and Y. Zhao, *Nat. Sustainability*, 2023, **6**, 1465–1473.

36 Q. Cheng, W. Chen, Y. Li and Y. Li, *Adv. Sci.*, 2024, **11**, 2307152.

37 U. Tiwari, J. Cole, Z. Li, A. Walton, L. P. Dwyer, B. F. Spencer, S. Zlatogorsky and K. L. Syres, *RSC Appl. Interfaces*, 2025, DOI: 10.1039/D5LF00206K.

38 F. Fan, Y. Zhang, M. Hao, F. Xin, Z. Zhou and Y. Zhou, *J. Energy Chem.*, 2022, **68**, 797–810.

39 P. Zhai, L. Ren, S. Li, L. Zhang, D. Li and S. (Frank) Liu, *Matter*, 2022, **5**, 4450–4466.

40 J. Cho, B. Kim, S. Ryu, A. J. Yun, B. Gil, J. Lim, J. Kim, J. Kim and B. Park, *Electron. Mater. Lett.*, 2023, **19**, 462–470.

41 C. Yang, W. Hu, J. Liu, C. Han, Q. Gao, A. Mei, Y. Zhou, F. Guo and H. Han, *Light: Sci. Appl.*, 2024, **13**, 227.

42 J. Klein, L. Kampermann, B. Mockenhaupt, M. Behrens, J. Strunk and G. Bacher, *Adv. Funct. Mater.*, 2023, **33**, 2304523.

43 C. C. F. Kumachang, D. I. Amune, I. M. Asuo, D. Sanni, Y. A. Olanrewaju, N. Doumit, R. Koech, V. Anye, E. Ntsoenzok and N. Y. Doumon, *Adv. Energy Sustainability Res.*, 2024, **5**, 2300258.

44 Y. Yang, Z. Huang, H. Gao, Z. Xu, W. Fang, Y. Chen, Y. Hu, Z. Yi, J. Huang and H. Zhu, *RSC Adv.*, 2024, **14**, 32370–32388.

45 E. J. Stallknecht, C. K. Herrera, C. Yang, I. King, T. D. Sharkey, R. R. Lunt and E. S. Runkle, *Sci. Rep.*, 2023, **13**, 1903.

46 Q. Chen, H. Zhou, T.-B. Song, S. Luo, Z. Hong, H.-S. Duan, L. Dou, Y. Liu and Y. Yang, *Nano Lett.*, 2014, **14**, 4158–4163.

47 T. J. Jacobsson, J.-P. Correa-Baena, E. Halvani Anaraki, B. Philippe, S. D. Stranks, M. E. F. Bouduban, W. Tress, K. Schenk, J. Teuscher, J.-E. Moser, H. Rensmo and A. Hagfeldt, *J. Am. Chem. Soc.*, 2016, **138**, 10331–10343.

48 Y. Gao, H. Raza, Z. Zhang, W. Chen and Z. Liu, *Adv. Funct. Mater.*, 2023, **33**, 2215171.

49 D. S. Mann, S. Thakur, S. S. Sangale, K.-U. Jeong, S.-N. Kwon and S.-I. Na, *Sol. Energy Mater. Sol. Cells*, 2024, **269**, 112768.

50 E. Han, J.-H. Yun, I. Maeng, T. Qiu, Y. Zhang, E. Choi, S.-M. Lee, P. Chen, M. Hao, Y. Yang, H. Wang, B. W. Zhang, J. S. Yun, J. Seidel, M. Lyu and L. Wang, *Nano Energy*, 2024, **131**, 110136.

51 B. Sharma, R. Garai, M. A. Afroz, T. Sharma, S. Choudhary, R. K. Singh and S. Satapathi, *Adv. Energy Mater.*, 2024, **14**, 2402473.

52 N. Yao, Y. Xia, Y. Liu, S. Chen, M. P. Jonsson and F. Zhang, *ACS Appl. Energy Mater.*, 2021, **4**, 14335–14341.

53 S. Rahmany and L. Etgar, *ACS Energy Lett.*, 2020, **5**, 1519–1531.

54 F. Qian, S. Yuan, L. Wang, T. Zhang, Q. Xu, T. Lan, P. Zhang, Q. Sun, Z. D. Chen and S. Li, *Nano Energy*, 2025, **140**, 111070.

55 A. Axelevitch, B. Gorenstein and G. Golan, *Phys. Proc.*, 2012, **32**, 1–13.

56 R. Liu, R. Yu and Z. Tan, *Nanomaterials*, 2025, **15**, 786.

57 Z. Wang, Z. Zhang, L. Xie, S. Wang, C. Yang, C. Fang and F. Hao, *Adv. Opt. Mater.*, 2022, **10**, 2101822.

58 K. Deng, Q. Chen, Y. Shen and L. Li, *Sci. Bull.*, 2021, **66**, 2362–2368.